

Banner appropriate to article type will appear here in typeset article

The bistability of curved compression ramp flows

Yan-Chao Hu^{1,2}†, Wen-Feng Zhou^{1,2}, Ming-Zhi Tang^{1,2}, Gang Wang^{1,2}, Ming Fang^{1,2}, Yan-Guang Yang^{1,3}‡, and Zhi-Gong Tang³

¹Laboratory of Aerodynamics in Multiple Flow Regimes, China Aerodynamics Research and Development Centre (CARD C), Mianyang 621000, China

²Hypervelocity Aerodynamics Institute, CARD C, Mianyang 621000, China

³CARD C, Mianyang 621000, China

(Received xx; revised xx; accepted xx)

This paper investigates the bistability of curved compression ramp (CCR) flows. It reports that both separated and attached states can be stably established even for the same boundary conditions, revealing that the ultimate stable states of CCR flows also depend on the initial conditions and evolutionary history. Firstly, we design a thought experiment involving two establishment routes of CCR flows, constructing two distinct-different stable states, respectively. Subsequently, three-dimensional direct numerical simulations are meticulously performed to instantiate the thought experiment, verifying the existence of the bistable states. Finally, we compare the pressure, wall friction, and heat flux distributions under two stable states. As a canonical type of Shock wave-Boundary layer interactions, local CCR flows often appear on aircraft, hence the bistability will certainly bring noteworthy changes to the global aerothermodynamic characteristics, which supersonic/hypersonic flight has to deal with.

Key words:

1. Introduction

In shock wave-boundary layer interaction (SBLI) flows, separation and attachment of boundary layers are the two most typical states (Babinsky & Harvey 2011). The ultimate stable states of a specific SBLI flow are widely considered to be unique for given inflow parameters and wall geometry, i.e., the boundary conditions. Although empirical, this understanding is still correct in most cases. However, in principle, effects of initial condition and evolutionary history of SBLIs can not be ignored, especially considering the reciprocal causation of shock wave (SW) patterns and boundary layer behaviors. An extreme question stemming from these process-dependent effects is that “can both stable separated and attached states exist for the same boundary conditions in *pure* SBLI flows?” The statement “*pure*” means that the flow is dominated by self-organized SBLIs rather than other multistable interactions, such as SW reflections (Ben-Dor *et al.* 2001; Tao *et al.* 2014). If the answer

† Email address for correspondence: huyanchao@cardc.cn

‡ Email address for correspondence: yangyanguang@cardc.cn

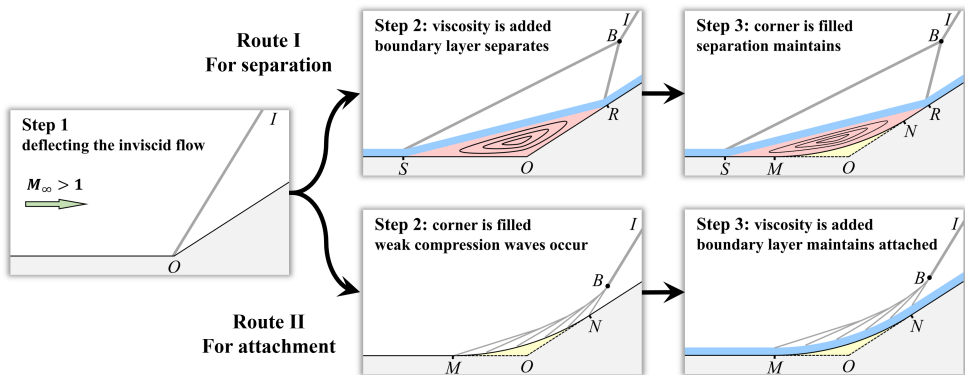


Figure 1: Two possible distinct-different (separation and attachment) stable CCR flows constructed via Route I and II.

is “yes”, the corresponding bistability will certainly bring significant differences to the aerothermodynamic characteristics, which is inevitable for super/hypersonic flight. Herein, a class of *pure* SBLI flows, the canonical compression ramp (CR) flows, are chosen to investigate the process-dependent effects, and their bistability is reported.

Large separated CR flows, classified as type VI of SW interactions by Edney (1968), are composed of large separation bubbles and λ -shock patterns. As a typical wall geometry, direct CRs (DCRs, the inclined ramp directly connecting the flat plate with one apex) are investigated widely, including the interaction processes with boundary layers’ distortions near separation (Chapman *et al.* 1958; Stewartson & Williams 1969; Neiland 1969), the aerodynamic characteristics (Gumand 1959; Hung 1973; Simeonides & Haase 1995; Tang *et al.* 2021), the vortex structures inside both the separation bubbles (Gai & Khraibut 2019; Cao *et al.* 2021) and the evolving boundary layers (Fu *et al.* 2021; Hu *et al.* 2017), and the unsteadiness of the SBLIs (Ganapathisubramani *et al.* 2009; Helm *et al.* 2021; Cao *et al.* 2021). On the other hand, due to the potential to weaken separation, curved CR (CCR, inclined ramp connecting the flat plate with curved walls) flows have gradually attracted the attentions of researchers (Tong *et al.* 2017; Wang *et al.* 2019; Hu *et al.* 2020). However, as far as we know, there are few reports about the multistability of *pure* SBLIs in the CR flows.

The rest of this paper is organized as follows. Sec. 2 describes a thought experiment to construct two distinct-different stable CCR flows for the same boundary conditions. Sec. 3 presents the three-dimensional (3D) direct numerical simulations (DNSs) to instantiate the thought experiment and verify the CCR flows’ bistability. Conclusions follow in Sec. 5.

2. Thought experiment

In this section, we design a thought experiment to construct two distinct-different stable CCR flows, separation and attachment, via Route I and II, respectively, as shown in Fig. 1.

First, a possible separated CCR flow is constructed via Route I with three steps.

- **Step 1: deflect the inviscid flow.** Set the initial flow field as an inviscid supersonic flow being deflected by a DCR geometry with ramp angle α . An oblique SW OI is formed and emits from the ramp apex O ;

- **Step 2: add the viscosity.** At some instant, the viscosity is suddenly added to the fluid. An attached boundary layer is subsequently formed and interacts with SW OI . For a large enough α , the attached boundary layer can not resist the strong adverse pressure gradient induced by SW OI and then separates from the wall. The inverse flow gradually shapes

a closed separation bubble SRO , deflecting both the attached boundary layer and the outer inviscid flow, and inducing two new SWs, SB and RB . As time goes on, the separation bubble stops growing and stabilizes, i.e., both the separation point S and the reattachment point R become almost fixed or only oscillate slightly;

- **Step 3: fill the corner into an arc.** The key to filling is to be slow, gentle and macroscopically continuous, ensuring that the flow is always in stable states during the filling process. Thus, we fill the corner O with an ‘imaginary machine’ that can produce solid wall material atom by atom. In order to minimize the disturbance, the time span between two fillings is longer than the relaxation time of the flow stabilization. In the end, the corner O is filled into an arc \overline{MN} (the yellow region) inside space SRO , and a stably separated CCR flow could be obtained, as shown in the end of Route I in Fig. 1.

Second, a possible attached CCR flow is constructed via Route II using three steps.

- **Step 1: deflect the inviscid flow.** This step is the same as Step 1 in Route I;
- **Step 2: fill the corner into an arc.** This step is similar to Step 3 in Route I, i.e., filling the corner into an arc (the yellow region). The only difference is that the corner’s filling comes before the fluid viscosity’s adding in Route II. Due to the curved wall \overline{MN} , SW OI emitting from point O is weakened to a series of compression waves spreading on \overline{MN} ;
- **Step 3: add the viscosity.** Similar to Step 2 in Route I, the viscosity is suddenly added to the fluid after the inviscid flow stably passing over the CCR in this step. Undergoing the weaker adverse pressure gradients of compression waves on \overline{MN} , the gradually formed boundary layer is very likely to stabilize at attached state, as shown in the end of Route II.

Compare Route I and II. Operationally, both stable separated and attached CCR flows could be obtained with three steps by only exchanging the order of their last two steps. However, in essence, the different presentations of the ultimate stable states originate from the emergence history of flow elements, including the boundary layer, SWs, and compression waves. In Sec. 3, 3D DNSs are performed to check the authenticity of the thought experiment.

3. Numerical experiment

In this section, the thought experiment shown in Fig.1 is numerically instantiated using 3D DNSs. The flow field in step 1 of can be obtained with the classical Rankine-Hugoniot relations. Therefore, only four steps need to be simulated: step 2 and 3 of both Route I and II. Details of DNS are in Sec. 3.1. Route I and II are instantiated in 3.2.2 and 3.2.3, respectively. Contrast of the bistable states is in Sec. 3.3.

3.1. Details of DNSs for DCR flows

3.1.1. Governing equations and numerical methods

The governing equations solved are dimensionless 3D Navier–Stokes equations for unsteady, compressible flow in curvilinear coordinates,

$$\frac{\partial \mathbf{Q}}{\partial t} + \frac{\partial (\mathbf{F}_c + \mathbf{F}_v)}{\partial \xi} + \frac{\partial (\mathbf{G}_c + \mathbf{G}_v)}{\partial \eta} + \frac{\partial (\mathbf{H}_c + \mathbf{H}_v)}{\partial \zeta} = 0, \quad (3.1)$$

where \mathbf{Q} is the conservative vector flux, \mathbf{F}_c , \mathbf{G}_c and \mathbf{H}_c are the inviscid convection fluxes, \mathbf{F}_v , \mathbf{G}_v and \mathbf{H}_v are the viscous fluxes. Here, \mathbf{Q} , \mathbf{F}_c and \mathbf{F}_v are defined as

$$\mathbf{Q} = J \begin{pmatrix} \rho^* \\ \rho^* \mathbf{U} \\ \rho^* e^* \end{pmatrix}, \mathbf{F}_c = J \begin{pmatrix} \rho^* \mathbf{U}^T \mathbf{J}_\xi \\ \rho^* \mathbf{U}^T \mathbf{J}_\xi \mathbf{U} + p^* \mathbf{J}_\xi \\ (\rho^* e^* + p^*) \mathbf{U}^T \mathbf{J}_\xi \end{pmatrix}, \mathbf{F}_v = J \begin{pmatrix} 0 \\ \frac{1}{\text{Re}_\infty} \boldsymbol{\tau} \mathbf{J}_\xi \\ \left(\frac{1}{\text{Re}_\infty} \mathbf{U}^T \boldsymbol{\tau} - \frac{1}{(\gamma-1) M_\infty^2 \text{Pr}} \mathbf{q}^T \right) \mathbf{J}_\xi \end{pmatrix}, \quad (3.2)$$

M_∞	Re_∞	h_0	u_∞	ρ_∞	T_∞	p_∞	T_w
7.7	(mm^{-1}) 4.2×10^6	(MJ kg^{-1}) 1.7	(m s^{-1}) 1726	kg m^{-3} 0.021	(K) 125	(Pa) 760	(K) 293

Table 1: The flow conditions based on the shock tunnel TH2 (Roghelia *et al.* 2017b).

where $\mathbf{J}_\xi = (\xi_x, \xi_y, \xi_z)^T$ are the metric coefficients and J is the determinant of the Jacobian matrix transforming the Cartesian coordinates (x, y, z) into the computational coordinates (ξ, η, ζ) . The velocity vector \mathbf{U} , the heat flux vector \mathbf{q} and the stress tensor $\boldsymbol{\tau}$ are defined as

$$\mathbf{U} = \begin{pmatrix} u^* \\ v^* \\ w^* \end{pmatrix}, \quad \mathbf{q} = \begin{pmatrix} q_\xi^* \\ q_\eta^* \\ q_\zeta^* \end{pmatrix}, \quad \boldsymbol{\tau} = \begin{pmatrix} \tau_{\xi\xi}^* & \tau_{\xi\eta}^* & \tau_{\xi\zeta}^* \\ \tau_{\eta\xi}^* & \tau_{\eta\eta}^* & \tau_{\eta\zeta}^* \\ \tau_{\zeta\xi}^* & \tau_{\zeta\eta}^* & \tau_{\zeta\zeta}^* \end{pmatrix}. \quad (3.3)$$

The total energy e^* is defined as

$$e^* = \frac{u^{*2} + v^{*2} + w^{*2}}{2} + \frac{1}{\gamma - 1} \frac{p^*}{\rho^*}. \quad (3.4)$$

The other four flux terms have the similar forms: \mathbf{G}_c and \mathbf{H}_c are similar in form to \mathbf{F}_c ; \mathbf{G}_v and \mathbf{H}_v are similar in form to \mathbf{F}_v . The viscosity μ is determined with the Sutherland's law, and perfect gas equation, relating the pressure p the density ρ and the temperature T , is used to close the equations set. The Prandtl number $Pr = 0.7$ and the specific heat ratio $\gamma = 1.4$ are chosen in the simulations. The non-dimensional variable are normalized using the inflow parameters: $\rho^* = \rho/\rho_\infty$, $u^* = u/u_\infty$, $v^* = v/u_\infty$, $w^* = w/u_\infty$, $T^* = T/T_\infty$, $e^* = e/u_\infty^2$ and $p^* = \rho^*T^*/(\gamma Ma_\infty^2)$. The reference length is chosen as 1 mm.

In terms of the numerical methods, the time integration is performed by the third-order TVD-type Runge–Kutta method; the inviscid fluxes are discretized by the fifth-order WENO method (Jiang & Shu 1996); the viscous fluxes are discretized with the sixth-order central difference scheme. The DNSs are conducted with the in-house code OPENCDFD-SC, whose capability has been well examined (Hu *et al.* 2017; Xu *et al.* 2021), [especially in studying compression ramp flows](#).

3.1.2. Wall geometry, flow parameters, mesh spacing and initial & boundary conditions

The choices of the compression ramp geometry (DCR) and the flow parameters are based on the recent shock-tunnel experiments (Roghelia *et al.* 2017a,b; Chuvakhov *et al.* 2017). As the DCR configuration shown in Fig. 2, the DCR configuration is mainly composed of two parts, the flat plate and the ramp, both of which have the same length $L = 100\text{mm}$ and width $W = 30\text{mm}$. The ramp angle is $\alpha = 15^\circ$. The flow parameters are shown in Tab. 1, including the Mach number $Ma_\infty = 7.7$, the Reynolds number $Re_\infty = 4.2 \times 10^6$, the velocity $u_\infty = 1726\text{m s}^{-1}$, the density $\rho_\infty = 0.021\text{kg m}^{-3}$, the temperature $T_\infty = 125\text{K}$ and the pressure $p_\infty = 760\text{Pa}$. The isothermal wall condition is used with $T_w = 293\text{K}$, since the run time of the shock tunnel is very short.

The computational domain, i.e., the mesh region, is shown in Fig. 3. The streamwise region is $-4\text{mm} \leq x \leq 196.6\text{mm}$ (the leading edge is at $x = 0\text{mm}$); the wall-normal height is 25 mm; the spanwise width is 30 mm. Two mesh resolutions, $1020 \times 250 \times 200$ (M1) and $1420 \times 250 \times 300$ (M2), are considered for time and grid convergence studies. Both M1 and M2 cluster the grids near the wall with the first wall-normal grid height being fixed to $\Delta y_w = 0.008\text{mm}$, yielding the non-dimensional height $\Delta y_w^+ \approx 0.3\text{mm}$ at $x/L \approx 0.5$.

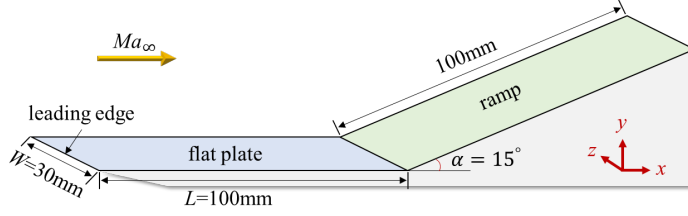


Figure 2: The schematic of the DCR configuration.

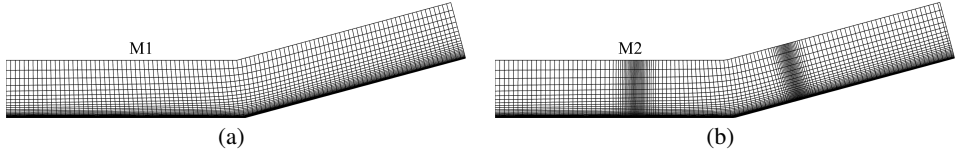


Figure 3: Mesh distributions in $x - y$ plane. (a) M1; (b) M2.

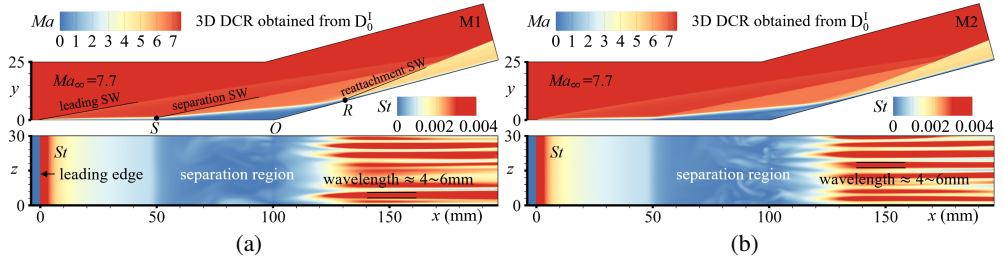


Figure 4: DNS results colored by local Mach number in $x - y$ plane and the Stanton number St in $x - z$ plane. (a) M1; (b) M2.

Spanwise grid spaces of both M1 and M2 are uniform, as $\Delta z = 0.15$ mm (M1) and 0.1 mm (M2). The streamwise grid spaces are uniform as $\Delta x_\xi = 0.2$ mm in M1. To investigate the pressure gradient effects, near the separation point $x_S/L \approx 0.55$ and the reattachment point $x_R/L \approx 1.28$ (also shown in Fig. 4) in M2, the Δx_ξ spaces are severally clustered with 200 points in the streamwise direction.

For the initial conditions, the initial flow fields for M1 and M2 are both **extruded (or extended)** spanwisely from the 2D simulation result (denoted as D_0^I), in which field the separation point $x_S/L \approx 0.55$ and the reattachment point $x_R/L \approx 1.28$. For the boundary conditions, the free stream is set both at the numerical inlet boundary ($x = -4$ mm) and the upper boundary; no-slip and isothermal ($T_w = 293$ K) conditions are set for $x \geq 0$ mm on the wall; the **extrapolation** condition is set at the outflow boundary.

3.1.3. Verification and validation

The 3D instantaneous flow fields of M1 and M2 are shown in Fig. 4. In the central $x - y$ planes, it clearly shows that the SW configurations include the leading edge SW, the separation SW, and the reattachment SW. In the first $x - z$ planes (on the wall), it can be noted that the wavelengths of the spanwise streaks on the ramp, colored by the Stanton number St defined in Eq. 3.5, are about 4 ~ 6mm, which are consistent with the previous experimental observations (Roghelia *et al.* 2017a,b; Chuvakhov *et al.* 2017) and numerical results (Cao *et al.* 2021). The aerothermodynamic characteristics are used to verify and validate the DNSs'

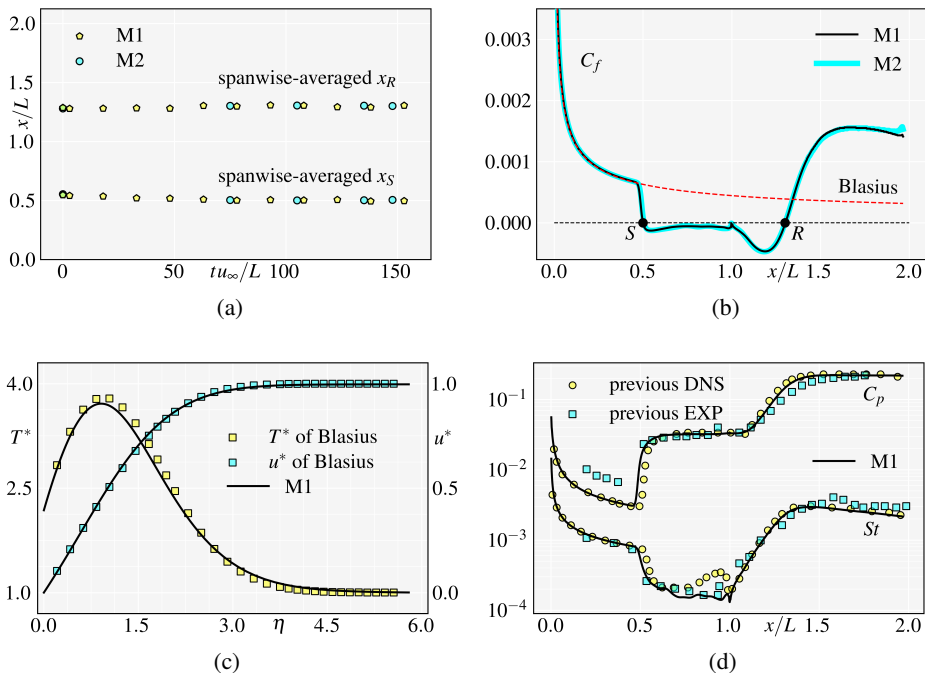


Figure 5: (a) Verifications of the time-convergence with variations of x_S and x_R ; (b) verification of the grid-convergence with C_f distributions, and validation with C_f on the flat-plate region; (c) validation with theoretical normal profiles of u and T ; (d) validation with C_p and St distributions of previous studies.

results, including the skin friction coefficient C_f , the surface pressure coefficient C_p , and the Stanton number St , which are defined as

$$C_f = \frac{\tau_w}{\frac{1}{2}\rho_\infty u_\infty^2}, \quad C_p = \frac{p_w - p_\infty}{\frac{1}{2}\gamma Ma_\infty^2 p_\infty}, \quad St = \frac{q_w}{\rho_\infty u_\infty c_p (T_{aw} - T_w)} \quad (3.5)$$

where τ_w , p_w and q_w are the friction, pressure and heat flux on the wall, respectively. c_p and T_{aw} are the specific heat capacity and the adiabatic wall temperature, respectively.

The verifications include the time- and grid-convergences. For the time-convergences, as shown in Fig. 5(a), the non-dimensional simulation time tu_∞/L of M1 and M2 are both longer than 145. It shows that the spanwise-averaged locations of the separation and reattachment points only oscillate slightly near $x_S/L \approx 0.5$ and $x_R/L \approx 1.3$ after $tu_\infty/L > 70$, implying the separated DCR flows have been stabilized in both M1 and M2. For the grid-convergence, as shown in Fig. 5(b), there are only small discrepancy of the C_f distributions between M1 and M2, implying the mesh resolution of M1 is suitable for the present simulations.

The validations include the comparisons of the present C_f , C_p , St distributions, and u^* , T^* profiles with the [accepted](#) theoretical, numerical and experimental results. The laminar boundary layer before separation is self-similar satisfying the Blasius theoretical solutions (White & Majdalani 2006). Fig. 5(b) shows the theoretical C_f distribution, and Fig. 5(c) shows the theoretical normal profiles of u^* and T^* at $x/L = 0.36$. It is noted that both the present C_f distribution and normal profiles agree well with the theoretical solutions, validating the simulations' accuracy. Furthermore, as shown in Fig. 5(d), the present C_p and St distributions are also compared with the previous experiment (Roghelia *et al.* 2017a;

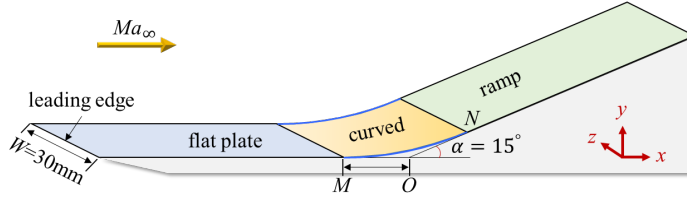


Figure 6: The schematic of the DCR configuration.

Chuvakhov *et al.* 2017) and DNS (Cao *et al.* 2021) results, and the excellent agreements validate the present DNSs.

3.2. DNSs for bistable states of CCR flows

3.2.1. Numerical strategy to realize the thought experiment

As mentioned in Sec. 2, “adding the viscosity” and “filling the corner” are the key operations to realize the thought experiment. In terms of “adding the viscosity”, the **implement** method is changing the governing equations from Euler to Navier-Stokes. In terms of “filling the corner”, since it requires to fill the corner macroscopically continuously (fill the corner atom by atom, microscopically), the strict operation is to manipulate the flow fields with an enormous number of steps, the number of which is the order of magnitude of the Avogadro number. Obviously, it is impossible in numerical simulation, and the equivalent implement is to replace the filling mode from ‘macroscopically continuous’ to ‘macroscopically discrete’. The specific strategy is as follows.

For Route I (“adding the viscosity” → “filling the corner”), the simulation process can be denoted as $D_0^I \rightarrow C_1^I \rightarrow C_2^I \rightarrow \dots \rightarrow C_N^I$, where the superscript ‘I’ denotes Route I, and the subscript ‘N’ represents the discrete number. Thus, D_0^I is the stable separated DCR flow in step 2, and C_N^I is the stable CCR flow after ‘N’ times of corner filling in step 3.

For Route II (“filling the corner” → “adding the viscosity”), the simulation process is denoted as $C_N^{II,inv} \rightarrow C_N^{II}$, where $C_N^{II,inv}$ is the inviscid CCR flow in step 2, and C_N^{II} is the stable viscous flow in step 3, with the expectation of maintaining attached.

3.2.2. Simulations of Route I

For $D_0^I \rightarrow C_1^I \rightarrow C_2^I \rightarrow \dots \rightarrow C_N^I$ (Route I), we set $N = 4$, and C_1, C_2, C_3, C_4 are four CCR configurations with curvature radiuses $R \approx 174.7, 189.9, 220.3, 227.9\text{mm}$ ($MO = 23, 25, 29, 30\text{mm}$), respectively. The four configurations’ meshes are set with the same resolution of M1 ($1020 \times 250 \times 200$). Three characteristic locations, x_S, x_R , and $x_{C_f, min}$, are considered to quantify the flow states variations, where $x_{C_f, min}$ denotes the locations of minimal C_f values in attached states. During process $D_0^I \rightarrow C_1^I \rightarrow C_2^I \rightarrow C_3^I \rightarrow C_4^I$, the evolutionary histories of spanwise-averaged x_S and x_R (red dashed lines) in C_1, C_2, C_3 , and C_4 are shown in Fig. 7(a), 7(b), 7(c), and 7(d), respectively, and the non-dimensional time $tu_\infty/L > 100$ (see the upper red x -axes) for all cases. Obviously, x_S and x_R in C_1, C_2 , and C_3 are all maintaining two branches for $tu_\infty/L > 200$, implying C_1^I, C_2^I , and C_3^I can all be stabilized at separated states. However, for C_4 (the largest curvature radius), x_S and x_R ultimately merge into one branch (the $x_{C_f, min}$ branch—the blue solid line) at $tu_\infty/L \approx 100$, implying C_4^I ends up in the attached state. Flow fields of C_1^I, C_2^I, C_3^I , and C_4^I are also shown in Fig. 9(a), 9(c), 9(e), and 9(b), respectively. It is noted that, on the ramp, the streaks in CCR are weaker than those in DCR.

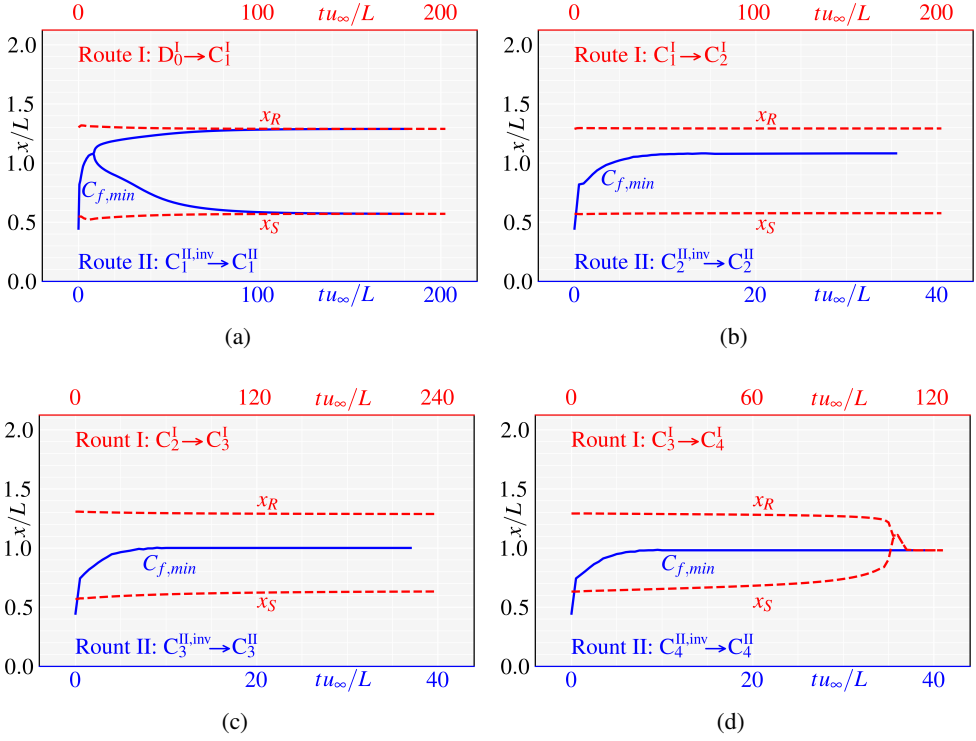


Figure 7: Convergence trajectories of x_S , x_R , and $x_{C_{f,min}}$ of Route I and II. (a) C_1^I and C_1^{II} ; (b) C_2^I and C_2^{II} ; (c) C_3^I and C_3^{II} ; (d) C_4^I and C_4^{II} .

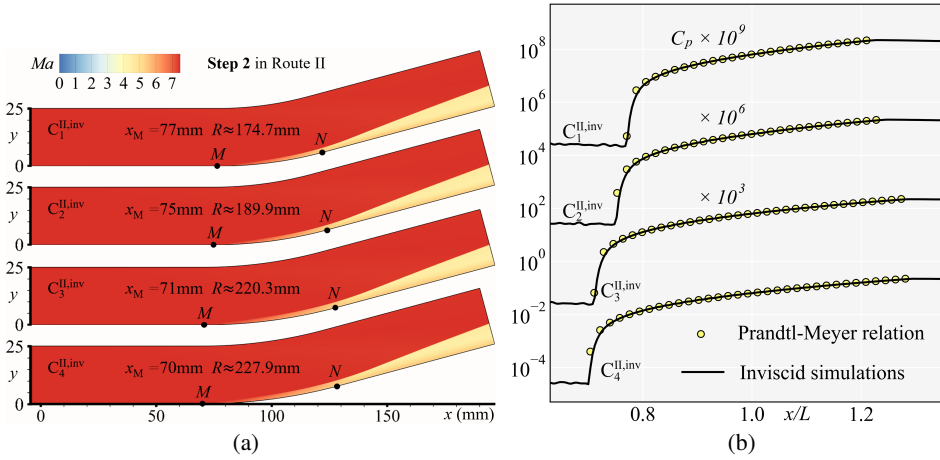


Figure 8: Simulations of $C_1^{II,inv}$, $C_2^{II,inv}$, $C_3^{II,inv}$, and $C_4^{II,inv}$ to reproduce Step 2 in Route II. (a) flow fields colored by local Mach number in $x-y$ plane; (b) validation with Prandtl-Meyer relation of C_p .

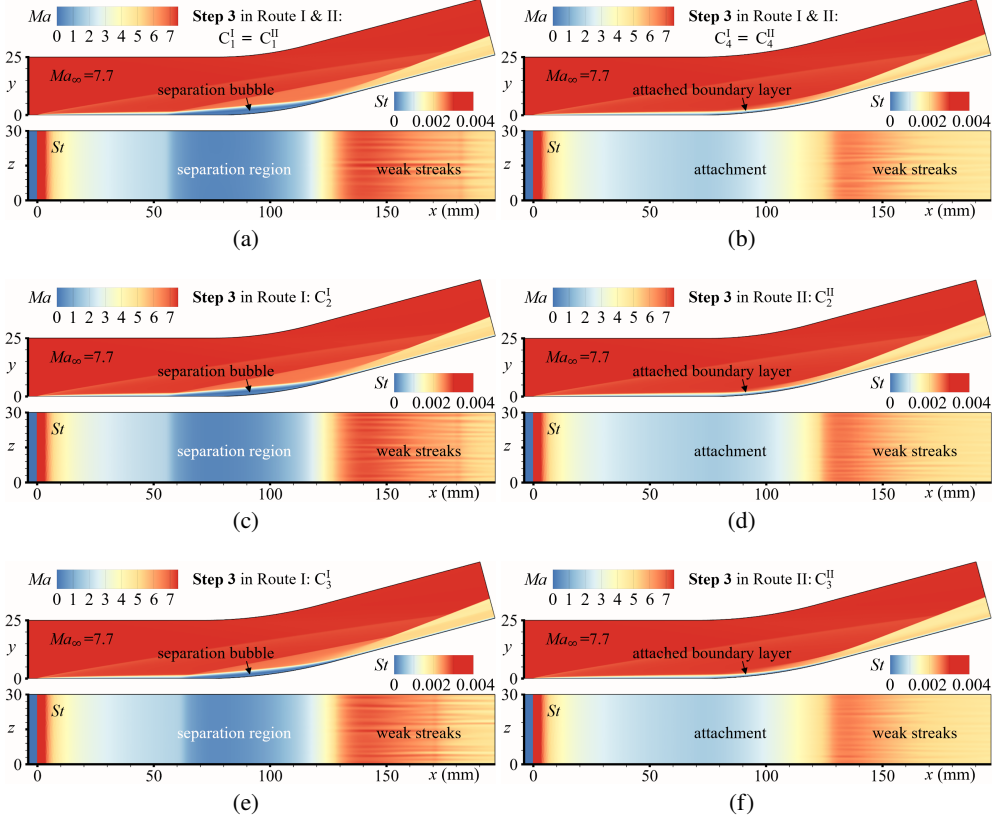


Figure 9: Terminuses of Route I and II. (a) C_1^I and C_1^{II} -separated; (b) C_4^I and C_4^{II} -attached; (c) C_2^I -separated; (d) C_2^{II} -attached; (e) C_3^I -separated; and (f) C_3^{II} -attached.

3.2.3. Simulations of Route II

For $C_N^{II,inv} \rightarrow C_N^{II}$ (Route II), the flows in Step 2 (inviscid flows in C_N , $N=4$) are simulated with Euler equations, which are shown in Fig. 8(a) and denoted as $C_1^{II,inv}$, $C_2^{II,inv}$, $C_3^{II,inv}$, and $C_4^{II,inv}$, respectively. A series of compression waves distribute on the curved wall \overline{MN} regions, and the C_p distributions on \overline{MN} satisfy the Prandtl-Meyer relations, as shown in Fig. 8(b), validating the present simulations.

To accomplish Step 3 in Route II (adding viscosity), Euler equations are replaced with Navier-Stokes form, with the expectation of obtaining the stable attached states. The processes are denoted as $C_1^{II,inv} \rightarrow C_1^{II}$, $C_2^{II,inv} \rightarrow C_2^{II}$, $C_3^{II,inv} \rightarrow C_3^{II}$, and $C_4^{II,inv} \rightarrow C_4^{II}$, whose evolutionary histories of $x_{C_f,min}$ are respectively shown in Fig. 7(a), 7(b), 7(c), and 7(d) (non-dimensional time $tu_\infty/L > 35$ for all cases, see the lower blue x -axes). $x_{C_f,min}$ -variations in C_2 , C_3 , and C_4 are similar: being of only one branch, first moving downstream and then stabilizing after about $tu_\infty/L \approx 10$. This behavior implies C_2^{II} , C_3^{II} , and C_4^{II} all ultimately stabilize in attached states. However, in C_1 (the smallest curvature radius), the $x_{C_f,min}$ bifurcates into two branches at $tu_\infty/L \approx 3$. The lower and upper branches respectively converge to the x_S and x_R branches obtained from $D_0^I \rightarrow C_1^I$, implying C_1^{II} finally stabilizes in the separated state. Flow fields of C_1^{II} , C_2^{II} , C_3^{II} , and C_4^{II} are also shown in Fig. 9(a), 9(d), 9(f), and 9(b), respectively.

C_1^I	C_1^{II}	C_2^I	C_2^{II}	C_3^I	C_3^{II}	C_4^I	C_4^{II}
Separated	Separated	Separated	Attached	Separated	Attached	Attached	Attached

Table 2: The ultimate states of the two routes in different configurations

3.3. Contrast of the bistable states

The ultimate states of route I and II are listed in Table 2. For configuration C_1 , the ultimate states, C_1^I and C_1^{II} , are both separated as shown in Fig. 7(a); for configuration C_4 , the ultimate states, C_4^I and C_4^{II} , are both attached as shown in Fig. 7(c). It needs to be emphasized that, for configurations C_2 and C_3 (Fig. 7(b) and 7(c)), both separated states (C_2^I and C_3^I in Fig. 9(c) and 9(e)) and attached (C_2^{II} and C_3^{II} in Fig. 9(c) and 9(d)) states can be stably established for the same boundary conditions, verifying the existence of the bistable states in CCR flows. The ultimate states of route I and II are listed in Table 2. **Also note that the weak streaks emerge in the downstream, implying the bistable states can resist disturbances of a certain intensity.**

According to the ultimate states, the solution space of the flow field can be divided into three regions by two critical curvature radii, R^A and R^S , as shown in Fig. 10(a): only stable attached states exist when $R > R^A$ (the overall attachment region); only stable separated states exist when $R < R^S$ (the overall separation region—the yellow area \mathcal{A}_S); both stable separate and attached states are physically possible when $R^A \leq R \leq R^S$ (the dual-solution region—the green area \mathcal{A}_D). The filled-area ratio η is used to characterize the relative proportions of the dual-solution region, which is defined as

$$\eta = \frac{\mathcal{A}_D}{\mathcal{A}_D + \mathcal{A}_S} = \frac{(R^A)^2 [\tan(\frac{\alpha}{2}) - \alpha] - (R^S)^2 [\tan(\frac{\alpha}{2}) - \alpha]}{(R^A)^2 [\tan(\frac{\alpha}{2}) - \alpha]} = 1 - \left(\frac{R^S}{R^A}\right)^2. \quad (3.6)$$

In the present cases, $\eta \geq 25.69\%$ with $R^S \leq R_2 = 189.9\text{mm}$ and $R^A \geq R_3 = 220.3\text{mm}$. In other words, during the filling process, more than a quarter of the materials “break” the one-to-one corresponding relations from the configuration geometries to the flow states.

Furthermore, the aerothermodynamic characteristics including the distributions of spanwise-averaged C_f , C_p and St on C_2 and C_3 are shown in Fig. 10. For both separated states (C_2^I and C_3^I) and attached (C_2^{II} and C_3^{II}) states of C_2 and C_3 , all the distributions of C_f collapse in the upstream part of the flat plate, so do C_p and St . However, in the downstream, the distributions are distinctly different. For the C_f distributions, as shown in Fig. 10(b), C_2^I and C_3^I quickly drop to negatives after separation and sharply rise to positives after reattachment, and both of them have two minimal values in the separation regions; while both C_2^{II} and C_3^{II} stay positive, and have only one minimal value, severally. For C_p distributions, as shown in Fig. 10(c), C_2^I and C_3^I present plateaus in the separation regions, rise sharply after reattachment and then reach peaks, severally; while both C_2^{II} and C_3^{II} continuously decrease till the starting points M of the curved walls, and then rise in the form of isentropic compression. For the St distributions, as shown in Fig. 10(d), C_2^I and C_3^I drop rapidly to near zero ($O(10^{-4})$) after separation, and then increase rapidly to the peaks; while C_2^{II} and C_3^{II} slowly decrease till the starting points M , and then increase gradually. Additionally, in the downstream of the ramps, C_f , C_p , and St of the separated states are all greater than those of the attached states.

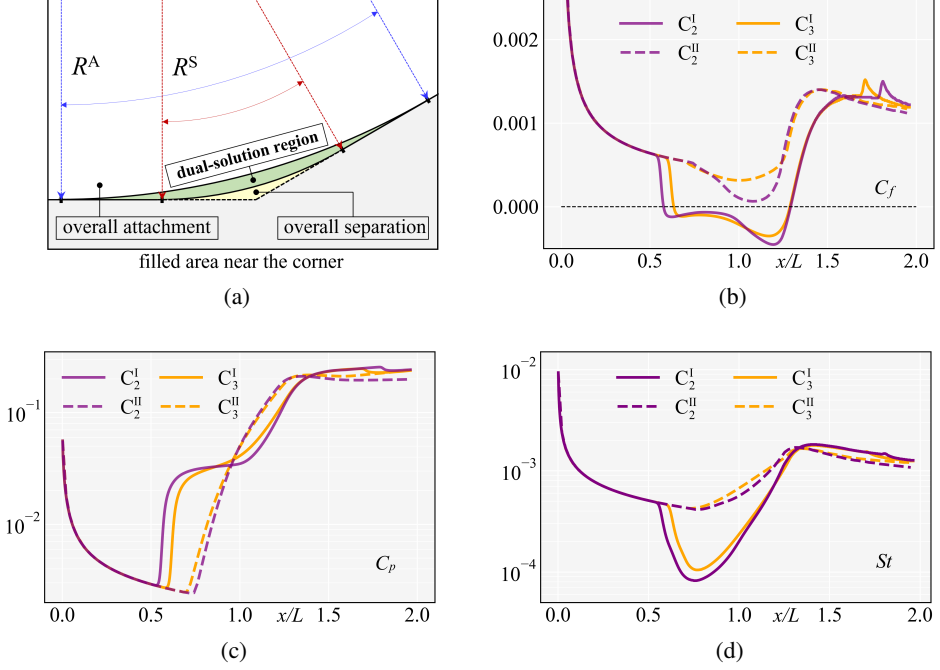


Figure 10: (a) Schematic of the solution regions; distributions of (b) C_f ; (c) C_p , and (d) St .

4. Robustness study

The phenomenon of bistability is somewhat counterintuitive, i.e., both separated and attached states can stably exist in C2 or C3 in the present cases, as shown in 2. To confirm its existence in the in the real physical world with disturbances, we further investigate the robustness of this phenomenon. Specifically, the attached states, C_2^{II} and C_3^{II} , are studied with some disturbances imparted to the upstream flow.

The disturbances have the following form, a region of steady blowing and suction, referring to Pirozzoli *et al.* (2004),

$$v(x, z, t) = Au_{\infty}f(x)g(z)h(t), \quad x_a \leq x \leq x_b, \quad (4.1)$$

with A the amplitude of the disturbance, u_{∞} the freestream velocity, and

$$\begin{aligned} f(x) &= 4 \sin \theta (1 - \cos \theta) / \sqrt{27}, \quad \theta = 2\pi(x - x_a) / (x_b - x_a), \\ g(z) &= \sum_{l=1}^{l_{\max}} Z_l \sin [2\pi l(z/L_z + \phi_l)], \quad \sum_{l=1}^{l_{\max}} Z_l = 1, \quad Z_l = 1.25Z_{l+1}, \\ h(t) &= 1. \end{aligned} \quad (4.2)$$

The locations $x_a = 15\text{mm}$ and $x_b = 20\text{mm}$ denote the beginning and the end of the disturbance region, respectively. Two amplitudes, $A = 1\%$ and 2% , are chosen to investigate the influence of the disturbance strengths. $L_z = 30\text{mm}$ is the spanwise width of the computational domain. ϕ_l is a random number ranging between 0 and 1. Three cases are considered, i.e., $A = 1\%$ & 2% for C_2^{II} and $A = 2\%$ for C_3^{II} , all of which are simulated for $tu_{\infty}/L \geq 15$, and the results shown below are all at $tu_{\infty}/L = 15$.

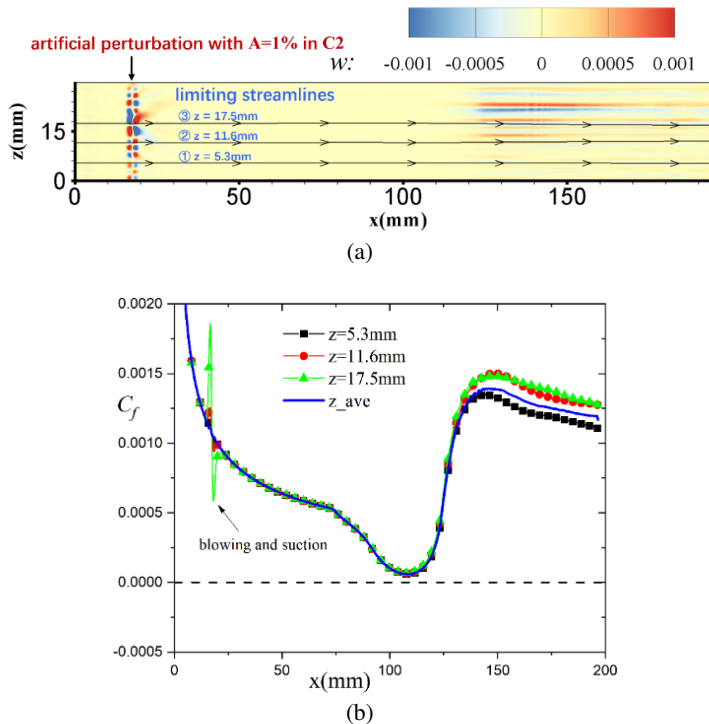


Figure 11: Simulations of $C_1^{\text{II,inv}}$, $C_2^{\text{II,inv}}$, $C_3^{\text{II,inv}}$, and $C_4^{\text{II,inv}}$ to reproduce Step 2 in Route II. (a) flow fields colored by local Mach number in $x - y$ plane; (b) validation with Prandtl-Meyer relation of C_p .

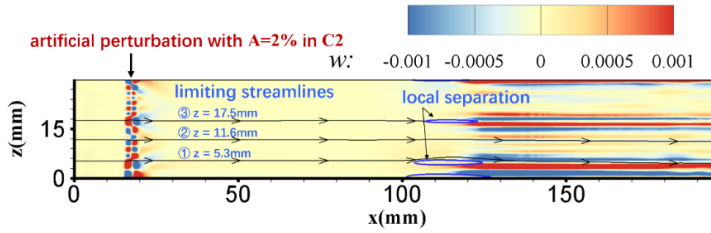
For C_2^{II} (the smaller curvature radius $R \approx 189.9\text{mm}$), the weaker disturbance ($A = 1\%$) can not perturb the attached state into a separated state, as shown in Fig. 11, while the stronger disturbance ($A = 2\%$) make the downstream boundary locally separate at $100\text{mm} \leq x \leq 125\text{mm}$, as shown in Fig. 12. This implies that the stable attached state in C2 can at least resist a disturbance with the amplitude of $1\%u_\infty$, and for a fixed shape, the weaker the disturbance, the less likely the attached state is to be broken.

For C_3^{II} (the larger curvature radius $R \approx 220.3\text{mm}$), even the stronger disturbance ($A = 2\%$) can not perturb the attached state into a separated state, as shown in Fig. 13. In fact, it can be seen that the C_f on the curved wall in C3 is larger (a greater distance from $C_f = 0$) than that of C2, which can resist a stronger disturbance. This implies that, for a certain disturbance, the larger the curvature radius, the more robust the attached state.

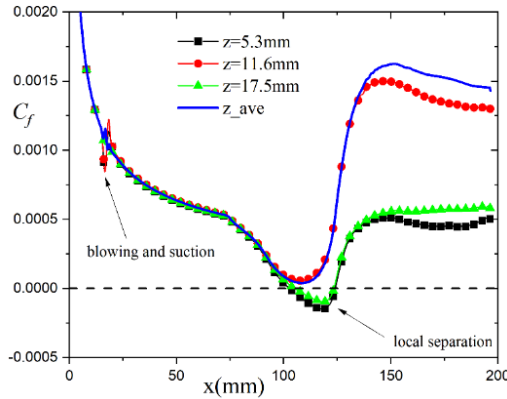
The above results imply that the bistable states can resist disturbances of a certain intensity; the larger the curvature radius, the more robust the attached state; the smaller the curvature radius, the more robust the separated state.

5. Conclusions

The CCR flows' bistability is conjectured through a thought experiment and verified using the 3D DNSs. The dual-solution region in the present cases accounts for more than 25 percent of the total filling area. The differences of bistable aerothermodynamic are compared. As an intrinsic property, CCR's bistability originates from the bifurcation characteristics of Navier-Stokes equations, and its specific presentation process can be diverse, corresponding to the hystereses induced by different parameter variations, such as Ma_∞ , α , and T_w - variations, and some 2D cases have been reported (Hu *et al.* 2020; Zhou *et al.* 2021).



(a)



(b)

Figure 12: Simulations of $C_1^{\text{II,inv}}$, $C_2^{\text{II,inv}}$, $C_3^{\text{II,inv}}$, and $C_4^{\text{II,inv}}$ to reproduce Step 2 in Route II. (a) flow fields colored by local Mach number in $x - y$ plane; (b) validation with Prandtl-Meyer relation of C_p .

Next, we will design wind tunnel experiments to show the bistable states of CCR flows, which is more interesting and challenging. After all, it took more than 100 years from Mach's discovery (Mach 1878) of two SW reflection patterns to the observation of their bistable states in the wind tunnel (Chpoun & Ben-Dor 1995). In some sense, there is systematic similarity between CCR flows and SW reflections: local subsonic regions (separation bubbles in CCR flows, and subsonic regions behind Mach stems in SW reflections) exist in the global supersonic/hypersonic flows, making the flow systems have both hyperbolic and elliptic characteristics. Therefore, the geometrical parameters, curvature radius R and wedge angle θ_w , play the similar role in the bistabilities of CCR flows and SW reflections, respectively.

SBLIs, represented by CCR flows, and Shock-Shock interactions (SSIs), represented by SW reflections (Ben-Dor *et al.* 2001), often dominate the complex flow in supersonic/hypersonic flight together. Therefore, more complex multistable shock patterns will be formed when multistable states of SBLIs and SSIs interact with each other, and the resultant complex aerothermodynamic characteristics need to be paid more attention in the future.

Acknowledgment

This work is supported by the National Key R & D Program of China (Grant No.2019YFA0405300). We look forward to receiving helpful comments from reviewers.

Declaration of interests. The authors report no conflict of interest.

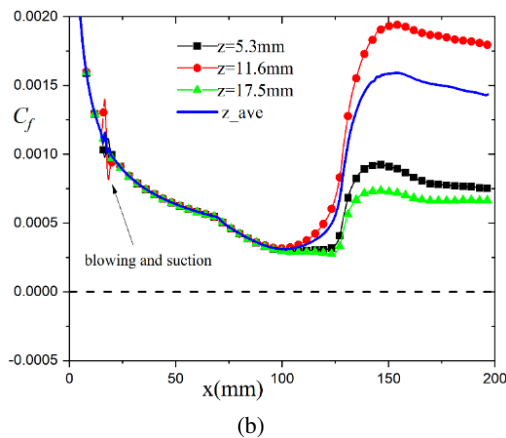
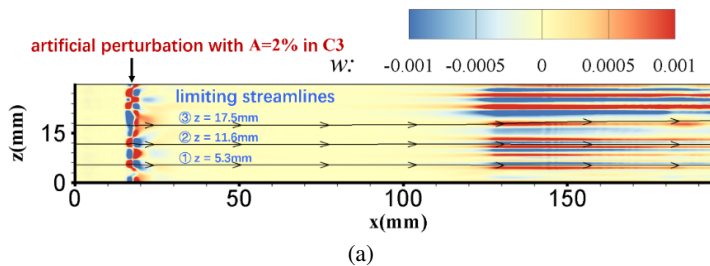


Figure 13: Simulations of $C_1^{\text{II,inv}}$, $C_2^{\text{II,inv}}$, $C_3^{\text{II,inv}}$, and $C_4^{\text{II,inv}}$ to reproduce Step 2 in Route II. (a) flow fields colored by local Mach number in $x - y$ plane; (b) validation with Prandtl-Meyer relation of C_p .

REFERENCES

- BABINSKY, H. & HARVEY, J. K. 2011 *Shock Wave-Boundary-Layer Interactions*.
- BEN-DOR, G., VASILIEV EI., ELPERIN, T. & CHPOUN, A. 2001 Hysteresis phenomena in the interaction process of conical shock waves: experimental and numerical investigations. *J. Fluid Mech.* **448**.
- CAO, S. B., HAO, J., KLIOUTCHNIKOV, I., OLIVIER, H. & WEN, C. Y. 2021 Unsteady effects in a hypersonic compression ramp flow with laminar separation. *J. Fluid Mech.* **912**.
- CHAPMAN, D. R., KUEHN, D. M. & LARSON, H. K. 1958 Investigation of separated flows in supersonic and subsonic streams with emphasis on the effect of transition .
- CHPOUN, A., PASSEREL D. LI H. & BEN-DOR, G. 1995 Reconsideration of oblique shock wave reflections in steady flows. part I. experimental investigation. *J. Fluid Mech.* **301**, 19–35.
- CHUVAKHOV, P. V., BOROVYOY, V. YA., EGOROV, I. V., RADCHENKO, V. N., OLIVIER, H. & ROGHELIA, A. 2017 Effect of small bluntness on formation of görtler vortices in a supersonic compression corner flow. *J. Appl. Mech. Tech. Phys.* **58** (6), 975–989.
- EDNEY, B. 1968 Anomalous heat transfer and pressure distributions on blunt bodies at hypersonic speeds in the presence of an impinging shock .
- FU, L., KARP, M., BOSE, S. T., MOIN, P. & URZAY, J. 2021 Shock-induced heating and transition to turbulence in a hypersonic boundary layer. *J. Fluid Mech.* **909**.
- GAI, S. L. & KHRAIBUT, A. 2019 Hypersonic compression corner flow with large separated regions. *J. Fluid Mech.* **877**, 471–494.
- GANAPATHISUBRAMANI, B., CLEMENS, N. T. & DOLLING, D. S. 2009 Low-frequency dynamics of shock-induced separation in a compression ramp interaction. *J. Fluid Mech.* **636**, 397–425.
- GUMAND, W. J. 1959 On the plateau and peak pressure of regions of pure laminar and fully turbulent separation in two-dimensional supersonic flow. *J. Aerosp. Sci.* **26** (1), 56–56.
- HELM, C. M., MARTÍN, M. P. & WILLIAMS, O. J.H. 2021 Characterization of the shear layer in separated shock/turbulent boundary layer interactions. *J. Fluid Mech.* **912**.

- HU, Y. C., BI, W. T., LI, S. Y. & SHE, Z. S. 2017 beta-distribution for reynolds stress and turbulent heat flux in relaxation turbulent boundary layer of compression ramp. *Sci. China: Phys., Mech. Astron.* **60** (12), 124711.
- HU, Y. C., ZHOU, W. F., WANG, G., YANG, Y. G. & TANG, Z. G. 2020 Bistable states and separation hysteresis in curved compression ramp flows. *Phys. Fluids* **32** (11), 113601.
- HUNG, F. T. 1973 Interference heating due to shock wave impingement on laminar boundary layers. In *6th Fluid and PlasmaDynamics Conference*.
- JIANG, GUANG-SHAN & SHU, CHI-WANG 1996 Efficient implementation of weighted eno schemes. *Journal of computational physics* **126** (1), 202–228.
- MACH, E. 1878 Über den verlauf von funkenwellen in der ebene und im raume. *Sitzungsbr. Akad. Wiss. Wien* **78**, 819–838.
- NEILAND, V. Y. 1969 Theory of laminar boundary layer separation in supersonic flow. *Fluid Dyn.* **4** (4).
- PIROZZOLI, SERGIO, GRASSO, F & GATSKI, TB 2004 Direct numerical simulation and analysis of a spatially evolving supersonic turbulent boundary layer at $m=2.25$. *Physics of fluids* **16** (3), 530–545.
- ROGHELIA, A., CHUVAKHOV, P. V., OLIVIER, H. & EGOROV, I. 2017a Experimental investigation of görtler vortices in hypersonic ramp flows behind sharp and blunt leading edges. *AIAA paper* p. 3463.
- ROGHELIA, A., OLIVIER, H., EGOROV, I. V. & CHUVAKHOV, P. V. 2017b Experimental investigation of görtler vortices in hypersonic ramp flows. *Exp. Fluids* **58**, 1–15.
- SIMEONIDES, G. & HAASE, W. 1995 Experimental and computational investigations of hypersonic flow about compression ramps. *J. Fluid Mech.* **283** (-1), 17–42.
- STEWARTSON, K. & WILLIAMS, P. G. 1969 Self-induced separation. *Proc. R. Soc. London, Ser. A* **312** (1509).
- TANG, M. Z., WANG, G., HU, Y. C., ZHOU, W. F., XIE, Z. X. & YANG, Y. G. 2021 Aerothermodynamic characteristics of hypersonic curved compression ramp flows with bistable states. *Phys. Fluids* **33** (12), 126106.
- TAO, Y., FAN, X. Q. & ZHAO, Y. L. 2014 Viscous effects of shock reflection hysteresis in steady supersonic flows. *J. Fluid Mech.* **759**, 134–148.
- TONG, F. L., LI, X. L., DUAN, Y.H. & YU, C. P. 2017 Direct numerical simulation of supersonic turbulent boundary layer subjected to a curved compression ramp. *Phys. Fluids* **29** (12), 125101.
- WANG, Q. C., WANG, Z. G., SUN, M. B., R.YANG, ZHAO, Y.X. & HU, Z. W. 2019 The amplification of large-scale motion in a supersonic concave turbulent boundary layer and its impact on the mean and statistical properties. *J. Fluid Mech.* **863**, 454–493.
- WHITE, F.M. & MAJDALANI, J. 2006 *Viscous fluid flow*, , vol. 3. McGraw-Hill New York.
- XU, D. H., WANG, J. C., WAN, M. P., YU, C. P., LI, X. L. & CHEN, S. Y. 2021 Effect of wall temperature on the kinetic energy transfer in a hypersonic turbulent boundary layer. *J. Fluid Mech.* **929**.
- ZHOU, W. F., HU, Y. C., TANG, M. Z., WANG, G., FANG, M. & YANG, Y. G. 2021 Mechanism of separation hysteresis in curved compression ramp. *Phys. Fluids* **33** (10), 106108.